BODIPY Chemisorbed on SnO₂ and TiO₂ Surfaces

for Photoelectrochemical Applications

Josephine A. Jayworth^{1,2,‡}, Cristina Decavoli^{1,2,‡}, Matt D. Capobianco^{1,2,3}, Jan Paul Menzel^{1,2}, Spencer R. Adler^{1,2}, Conrad A. Kocoj^{2,4}, Jessica G. Freeze^{1,2}, Robert H. Crabtree^{1,2}, Peijun Guo^{2,4}, Victor S. Batista^{1,2}, and Gary W. Brudvig^{1,2}*

¹Department of Chemistry, Yale University, New Haven, Connecticut, 06520, USA

²Yale Energy Sciences Institute, Yale University, West Haven, Connecticut, 06516, USA

³Department of Chemistry and Biochemistry, California State Polytechnic University, Pomona,

California, 91768, USA

⁴Department of Chemical and Environmental Engineering, Yale University, New Haven, Connecticut, 06520, USA

[‡] JAJ and CD contributed equally

*Corresponding Author: gary.brudvig@yale.edu

Keywords: BODIPY, electron injection, surface attachment, photosensitizer, photophysics, interfacial electron transfer

Abstract:

Advancement toward dye-sensitized photoelectrochemical cells to produce solar fuels by solardriven water splitting requires a photosensitizer that is firmly attached to the semiconducting photoelectrodes. Covalent binding enhances the efficiency of electron injection from the photoexcited dye into the metal oxide. Optimization of charge transfer, efficient electron injection, and minimal electron-hole recombination are mandatory for achieving high efficiencies. Here, a BODIPY-based dye exploiting an innovative surface-anchoring mode via boron is compared with a similar dye bound by a traditional carboxylic acid anchoring group. Through terahertz and transient absorption spectroscopic studies, along with GFN-xTB calculations, we find that, when compared to the traditional carboxylic acid anchoring group, electron injection of boron-bound BODIPY is faster into both TiO₂ and SnO₂. Although the surface coverage is low compared with carboxylic acids, the binding stability is improved over a wide range of pH. Subsequent photoelectrochemical studies using a sacrificial electron donor showed this combined dye and anchoring group maintained photocurrent with good stability over long-time irradiation. This recently discovered binding mode of BODIPY shows excellent electron injection and good stability over time, making it promising for future investigations.

Introduction:

New technologies that exploit solar radiation are required to reduce the use of fossil fuels. Artificial photosynthesis, the conversion of solar energy and water into fuels, is a popular solution for the storage of renewable energy in chemical bonds, addressing the intermittency issue of traditional solar-to-electricity technologies. Dye-sensitized photoelectrochemical cells (DSPECs) utilize photosensitizers along with catalysts to perform water oxidation at the photoanode and solar fuel evolution at the photocathode. These photoelectrodes are typically made of semiconductor oxides that favor charge transfer. The water oxidation reaction requires a 1.23 eV thermodynamic potential plus the applicable overpotential to overcome the high kinetic barriers involved, and among the materials suitable for this purpose are large bandgap semiconductors. However, this requirement greatly reduces the number of suitable materials, many of which have a limited absorption of solar radiation, making the use of visible-light photosensitizers highly desirable. Stability over time is a key feature that influences efficiency, so both the photoanode and photocathode require robust attachment of the photosensitizers onto the semiconductor electrodes. However, the semiconductor electrodes.

Molecular sensitizers have become important in the design of devices for solar driven production of solar fuels due to their facile tunability, versatility, and low cost.⁷⁻⁹ These molecules can be attached to the wide bandgap semiconductors via direct adsorption, π - π stacking, entrapment, or covalent anchoring.¹⁰ The latter strategy can often provide greater stability than the others,¹² but most photosensitizers require the introduction of special anchoring groups for stable binding on metal oxides.^{10,13,14} These groups often need to be attached at a late stage of the synthesis, hence our interest in avoiding this step.

Carboxylic and phosphonic acids are the most frequently used anchoring groups in DSPECs. ^{10,11} Carboxylic acids are employed mainly due to their high surface coverage, relatively easy synthesis, and efficient electron injection, while phosphonic acids due to their flexibility of binding mode which enhances their stability at neutral pH, despite the moderating effect on electron injection of the tetrahedral geometry at phosphorus and the lack of conjugation. However, both carboxylic and phosphonic groups easily undergo hydrolysis of the bond to the surface in the alkaline aqueous solutions often preferred for water oxidation reactions. In those conditions, the silatrane and hydroxamic groups provide a more robust bond with the surface of the semiconductor. ¹⁰ Silatrane-derived siloxane anchoring groups show limited electron injection into the semiconductor, making them more suitable for the anchoring of catalysts rather than photosensitizers. On the other hand, hydroxamate anchoring groups allow good electron injection into titanium dioxide, ¹⁵ but their multistep synthesis and exclusive preference for TiO₂ binding have limited their applications in many photosystems. ¹³

We recently discovered that BODIPY (4-difluoro-4-bora-3a,4a-diaza-s-indacene) molecules can covalently bind to TiO_2 without the need for any added surface-binding group. This binding occurs through the boron atom and the covalently bound BODIPY then efficiently injects electrons into TiO_2 upon photoexcitation. Successful binding requires the 3 and 5 positions of the molecule to be unsubstituted (Figure 1). Since molecules of the BODIPY family have seen wide use as photosensitizers for solar fuels production, $^{14,17-20}$ we have now investigated the electron injection mechanism into different metal oxides by comparison of two BODIPY dyes, one of which is bound by the traditional carboxylate group and the other via the boron. The two dyes are (T-4)-Difluoro[2-[phenyl(2H-pyrrol-2-ylidene- κN)methyl]-1H-pyrrolato- κN]boron (1) and (T-4)-Difluoro[4-[(5-methyl-1H-pyrrol-2-yl- κN)(5-methyl-2H-pyrrol-2-ylidene- κN)methyl]benzoic

acid]boron (2), which contains the same 8-phenyl-dipyrrin backbone and BF₂ group of 1. To ensure binding of 2 only through the carboxylic acid, two methyl groups were added in the 3 and 5 positions of the pyrroles to block binding via boron (Figure 1). In this way, we were able to individually evaluate and characterize the two different binding strategies to semiconductor surfaces using spectroscopic, theoretical, and photoelectrochemical methods.

The electrochemical, photophysical, and interfacial electron transfer properties were studied by steady-state absorption and emission spectroscopies as well as terahertz (THz) and time-resolved transient absorption (TA) spectroscopies. A semi-empirical quantum classical approach, that combines GFN-xTB based nuclear dynamics with quantum dynamics for the photoexcited electron and allows for tracking the electron injection in real time, was used to evaluate the interfacial electron transfer pathway between the photosensitizers and the metal oxides. The photoelectrocatalytic behavior was investigated in dye-sensitized photoanodes in the presence of a sacrificial electron donor (SED) to regenerate the oxidized species. The stability of the two binding modes was estimated both under non-illuminated aqueous conditions and under long-time irradiation. Finally, we looked at optimizing the loading of 1 onto the metal oxide surface by including different additives in the sensitizing solutions.

Figure 1. Molecular structure of the investigated compounds. The IUPAC numbering system for BODIPY dyes is included in green. Compound 1 binds via the boron and compound 2 via the carboxylate.

Experimental Methods:

Synthesis of Molecules and Films

Both molecules **1** and **2** were synthesized following previously reported procedures. ^{21,22} Briefly, a condensation reaction between benzaldehyde and pyrrole was run using indium chloride as the acid to create a dipyrromethane intermediate. Following workup, the dipyrromethane was oxidized using 2,3-dichloro-5,6-dicyano-1,4-benzoquinone to form the dipyrromethene to which boron trifluoride was added in the presence of triethylamine in dichloromethane. Both molecules were purified first by silica pad to remove most of the poly-pyrrole then column chromatography to obtain the pure product. Final products were confirmed by NMR and UV-visible spectroscopy and match the literature (see section S8 in the SI).

All TiO₂ films were made using a commercially available paste from Solaronix and the SnO₂ paste was made by modifying a reported procedure for a TiO₂ paste.²⁴ All films were prepared via the doctor blading method and annealed in a muffle furnace at 470 °C.¹⁶ This method was consistent for the films made on quartz, glass, and fluoride doped tin oxide (FTO) coated glass substrates.

Sensitizations of the films required 5 mM solutions of either 1 or 2 in anhydrous acetonitrile in oven dried glassware. These dry conditions proved to be of particular importance for the successful loading of 1. The metal oxide films were then submerged in the solutions and sealed in the vial at room temperature. Unless otherwise stated, all films sensitized with 1 were soaked for 20 hours and all films with 2 were soaked for one hour. As shown in Figure S1, a longer loading time does not increase the loading or the stability of 2 on TiO₂. It was not possible to obtain the dye loading via desorption methods due to the high stability of 1 on TiO₂ (see *Stability in Acidic*

and Basic Environments). Conditions which were successful in removing 1 from the surface resulted in either degradation of the molecule or dissolving the metal oxide. Therefore, surface loading was quantified using measurements of the solid films.

Optical and Electrochemical Characterizations

The UV-visible absorption spectra were measured using a Shimadzu UV-2600 UV-visible spectrophotometer. The spectra were measured in acetonitrile at a ~10 μM concentration for the solution species and an integrating sphere was used for the dye-sensitized films. Fluorescence emission spectra were measured on a Horiba Scientific FluoroMax Plus fluorophotometer. The excited-state potentials of the solubilized molecules were calculated using the intersection of the normalized absorbance and emission spectra to determine the 0-0 excitation energy together with a measurement of the ground state potential by cyclic voltammetry (CV). CV and differential pulse voltammetry (DPV) were performed with a Pine WaveNow potentiostat. The experiments were carried out in acetonitrile using tetrabutylammonium hexafluorophosphate (TBAPF₆) as the electrolyte. Boron doped diamond (BDD) disk, silver wire, and platinum wire were used as the working electrode, the pseudo-reference electrode, and the counter electrode, respectively. Ferrocenium/ferrocene was used as an internal standard. All CVs are adjusted to be referenced versus normal hydrogen electrode (NHE) and measured with a scan rate of 100 mV/s. All DPVs used a pulse of 5 mV height, 100 ms width, 500 ms period and 5 mV increment.

Quantum Chemistry Calculations

A semi-empirical quantum classical approach has been used to model the electron injection from the photoexcited BODIPY dyes into TiO_2 . This approach, which is a combination of quantum dynamics based on an Extended Hückel Hamiltonian for the photoexcited electron and *a priori* generated nuclear trajectories obtained by using semi-empirical molecular dynamics,

permits the simulation of photoinduced electron injection in extended systems, taking nuclear dynamics into account. It has previously successfully been applied to model electron injection from NDI based dyes into TiO2 as well as charge separation in push-pull dyes.^{28,29} Structure optimization and nuclear dynamics were performed using the DFTB+ program (version 22.2),³⁰ with GFN-1xTB as electronic structure method.³¹ Detailed information on the construction of the simulation box and computational settings can be found in the SI. The binding mode of 2 is predicted to be bidentate via its carboxylic acid group with surface Ti atoms, while 1 was attached via a B-O-Ti link, representing a nucleophilic attack of a surface hydroxide on the boron center, releasing a fluoride and proton in the process. A more detailed look into the adsorption mode is given in the SI. To equilibrate the system to room temperature, equilibration runs of 5 ps with a 1 fs time step were performed at the NVT (number, volume, temperature) ensemble using a Nosé-Hoover chain and a temperature of 293 K.32 The obtained geometries and velocities have been used as starting points to perform 10 trajectories of 250 fs each with a smaller time step of 0.1 fs in the NVE (number, volume, energy) ensemble that was used in the quantum dynamics. The quantum dynamics were performed using the AO/MO propagator²⁶ and an Extended Hückel Hamiltonian, which allows for optimization of the Hückel parameters such that they reproduce experimental redox potentials. The target values and optimization procedures as well as the obtained Hückel parameters can be found in section S7 in the SI. The initial wave packet representing the excited electron was chosen as the fragment LUMO of the respective dye molecule. The population on the respective fragments was obtained after performing the quantum propagation using a 0.1 fs time step on all a priori generated nuclear trajectories. The average over all 10 trajectories allows the mean populations over time to be obtained as well as standard deviations. The estimates for the electron injection rates were extracted from the slopes of a linear fit of the semi-logarithmic plot of these populations over time.

Optical Pump Terahertz Probe (OPTP) Spectroscopy

Ultrafast charge injection dynamics were studied using OPTP spectroscopy, of which the specific instrumentation and experimental techniques are described in depth in our previous publications.^{33,34} Samples of 1 and 2 were deposited onto ~4 µm thick films of SnO₂ onto quartz slides. Measurements were performed using a Ti:sapphire laser system (Spectra-Physics Spitfire Ace, 35 fs pulse width, 1 kHz repetition rate, 800 nm). For OPTP, the 800 nm fundamental pulse is partitioned into THz generation, detection, and photoexcitation beams. The THz pulse is generated via creating an air plasma, which is formed through frequency doubling to 400 nm of the THz generation beam, followed by its combination with the residual 800 nm light and focusing the two frequencies. Subsequently, the detection beam tracks the THz pulse amplitude using electro-optical sampling in a ZnTe (110) crystal.³⁵ The optical photoexcitation was done at 400 nm which was generated through frequency doubling the fundamental in a β-barium borate crystal. The time-delay between the optical and THz pulses was controlled by a mechanical delay stage. Samples were excited at 400 nm, and the change in peak THz is tracked over time (t_{pump}) due to the photoexcitation which can be attributed to electron injection. The OPTP traces were modeled according to a stretched exponential for electron injection and single exponential for recombination in the metal oxide as seen in Equation 1, where $\Delta THz(t)$ is the percent change in transmitted terahertz as a function of time, t_0 is the time of the pump pulse, a_i is the amplitude of charge injection, β is a "stretch" factor quantifying the heterogeneity of electron injection processes, t_i is the lifetime of electron injection, a_r is the amplitude of recombination, t_r is the

lifetime of charge trapping or recombination, y_{θ} is the y-axis offset, and $G_r(FWHM)$ is the Gaussian function of the instrument response time.^{21,36}

$$\Delta THz(t) = \left[a_i \left(1 - e^{-\left[\frac{-t - t_0}{t_i} \right]^{\beta}} \right) + a_r \left(e^{-\frac{t - t_0}{t_r}} \right) + y_0 \right] \otimes G_r(FWHM) \qquad [Equation 1]$$

The average electron injection lifetimes $\langle t_i \rangle$ were computed according to Equation 2.35

$$< t_i > = \frac{t_i}{\beta} \cdot \Gamma\left(\frac{1}{\beta}\right)$$
 [Equation 2]

Transient Absorption Studies

The transient absorption studies were conducted using white light supercontinuum probe pulses produced by focusing a portion of the 1030 nm output of a Pharos Light Conversion amplifier, with a repetition rate of 2 kHz and pulse duration of 170 fs, onto a 4 mm sapphire crystal. These probe pulses were delayed by a mechanical delay line and focused onto the sample by a concave mirror. The probe light that transmitted through the samples was focused into a fiber and routed to an AvaSpec-ULS2048CL-EVO spectrometer. The 400 nm pump pulses were produced by sending 800 nm pulses from an Orpheus optical parametric amplifier powered by the same Pharos amplifier through a second harmonic generation crystal. The pump beam was focused by a lens into a 280 µm spot size on the samples, which were mounted in a Janis VPF-100 liquidnitrogen cryostat and held at 78 K under a vacuum of 1 x 10⁻⁴ mbar. The pump spot size was measured using a 200 µm diameter pinhole, assuming a Gaussian-shaped beam. A home-built LabView program was used to collect the transient absorption spectra data by taking the difference between the transmittance of the samples with the pump blocked and unblocked by an optical chopper operating at 1 kHz and normalized by the transmittance with the pump blocked. 1 and 2 were deposited on ~4 μm thick films of SnO₂ on glass using the same conditions as for the THz films. The fluence incident upon the sample was 0.6 mJ cm⁻².

Stability Studies

Stability studies were conducted in solutions which were all made to be 0.1 M KCl with the pH then adjusted to pH 2, 7 or 10 using HCl and Na₂CO₃. Stability was monitored by taking UV-visible spectra of the films after 1, 3, 6 and 24 hours in the various solutions. The reported points have been replicated over 2 or 3 films.

Photoelectrochemistry Studies

Photoelectrochemistry experiments were conducted in aqueous solutions using sodium sulfite (Na₂SO₃) as a sacrificial electron donor. The electrolyte chosen was either 0.1 M phosphate buffer or 75 mM phosphate buffer with 25 mM sodium sulfite to maintain the same ionic strength in all the measurements. The working electrode was either 1 or 2 loaded onto a mesoporous TiO₂ film on a FTO coated glass substrate. The counter electrode was a platinum wire, and the reference electrode was Ag/AgCl. A 300 W xenon light was filtered through a 420 nm long pass filter giving a power of 100 mW cm⁻². Linear sweep voltammetry was conducted under 2-second chopped illumination and scan rate of 50 mV s⁻¹. A bias of 0 V vs Ag/AgCl was used for all the chronoamperometry (CA) measurements. The short CA measurements were performed with 50 seconds of 10 second chopped illumination followed by four minutes of continuous white light irradiation. The long CA measurements were performed with 5 minutes of 1 minute chopped illumination followed by 2 hours of continuous white light irradiation.

Loading Studies

Additives were tested during the loading of **1** and **2** by including an additional compound at 1 mM concentration to the 5 mM solution of **1** or **2** in MeCN. These additional compounds were glacial acetic acid (AcOH), 3,5-bis(trifluoromethyl)phenol (PhenolCF₃), *N,N*-diisopropylethylamine (DIPEA), 1,4-diazabicyclo[2.2.2]octane (DABCO), and

tetrabutylammonium fluoride trihydrate (TBAF). In all these experiments, a large solution of 5 mM 1 or 2 was made and divided among the different experiments with one experiment having no additive for an internal control. The UV-visible spectra of the films following a 20-hour sensitization were measured to determine a difference in loading. Glacial AcOH 99.7% has been purchased from JT Baker, PhenolCF₃ from Oakwood Chemical, DIPEA 99% from BeanTown Chemical, DABCO 98% from TCI and TBAF trihydrate 99% from Acros.

Results and Discussion:

Photophysical and Electrochemical Properties

Molecular sensitizers are the light-harvesting centers of DSPECs and thus convert photons into electron/hole couples. They should be highly absorbing in the visible/near infrared region of the solar spectrum, have a large enough bandgap to drive water oxidation and at the same time, inject electrons into the conduction band of the semiconductor.⁸ The absorption and extinction coefficients of **1** and **2** have been previously reported.¹⁶ The absorption spectra of the radical cations were also collected via spectroelectrochemistry (Figure S2). The fluorescence spectra for both molecules in MeCN solution are shown in Figure S3. All relevant optical and electrochemical data are displayed in Table 1.

Table 1. Optical and electrochemical parameters.

	λ_{\max} in $soln^a$ (nm)	λ_{\max} on films ^b (nm)	$\lambda_{\rm ems}^{a}$ (nm)	$\varepsilon^{a,c}$ (M ⁻¹ cm ⁻¹)	V_{ox}^{d} $\pm 10 \text{ mV}$ (V vs NHE)	E ₀₋₀ ^e (eV)	λ_{\max} radical cation $f(nm)$
1	344, 497	508	523	57,000	1.76	2.43	314, 500
2	330, 511	526	535	120,000	1.51	2.38	262, 458

 a in MeCN solution. b on TiO₂ films. c values at $\lambda_{max} \sim 500$ nm from ref. 15. d The potentials have been recorded in 0.1 M TBAPF₆ MeCN solution vs Fc⁺/Fc and reported after the conversion to NHE considering Fc⁺/Fc $_{(MeCN)}$ vs NHE = +0.63 V. 36 e calculated using intersection of normalized absorbance and emission. 20 f determined with spectroelectrochemistry in 0.1 M TBAPF₆ MeCN solution.

The methyl groups in the 3,5 positions of 2 drastically enhance the molar extinction coefficient increasing the planarity of the structure and affecting the HOMO-LUMO energies. 38-40 Additionally, the electron donating nature of the methyl groups leads to a slight stabilization of the radical cation and a less oxidizing wave in the CV when compared to 1 (Figure S4). The potentials for oxidation to form the radical cations were obtained using DPV (Figure S5) due to the irreversible features in the CV and are listed in Table 1. The 0-0 transition energies were extracted from the intersection of the normalized absorption and fluorescence spectra (Figure S3). All these parameters, as well as the conduction band levels for TiO₂ and SnO₂, and water oxidation potential are compared in Figure 2. From these values, we can see that both 1 and 2 are able to inject electrons from their excited state into TiO₂ and SnO₂ leaving a radical cation species with a potential oxidizing enough to drive water oxidation.

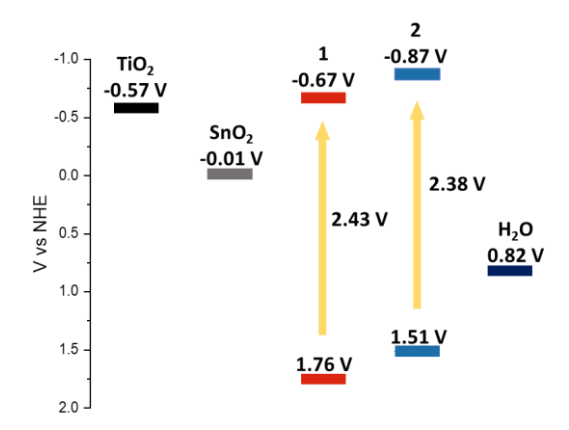


Figure 2. Schematic of the energy levels of **1** and **2** compared to the conduction bands of TiO₂ and SnO₂ and the water oxidation potential adjusted to pH 7.

Electron Injection Measurements

For a photosensitizer to be effective in a DSPEC photoanode it is critical that electron injection is efficient and charge recombination is suppressed.⁵ For this purpose, electron injection is well known to be rapid with carboxylic acid anchoring groups compared with other common ones.¹⁰ The electron injection of **1** and **2** into TiO₂ has already been reported as measured by

terahertz spectroscopy.¹⁵ This provides good evidence that the LUMO of these molecules is positioned appropriately for electron injection into the conduction band of TiO₂ when irradiated by visible light. However, the electron injection into TiO₂ was found to occur faster than the instrument response time of 0.40 ps. To better understand charge carrier dynamics, SnO₂ was substituted as the semiconductor since it gives slower electron injection compared with TiO₂.³⁸ The loading ration of 1 vs 2 on SnO₂ is similar to that on TiO₂ (Figure S6). Figure 3 and Table 2 show how SnO₂ allows for computational modeling and comparison of electron injection kinetics for 1 and 2.

Figure 3 displays the OPTP electron injection data with square markers for %ΔTHz, which is the peak THz amplitude at a given time relative to the pre-photoexcited amplitude. OPTP traces were fitted with the function described in Equation 1 (see Experimental Methods), plotted in Figures S5-S8 with all the fitting parameters reported in Table 2 and Table S1. The average electron injection lifetimes in Table 2 show that 1 indeed injects into SnO₂ faster than 2, presumably because the LUMO of 1 is located closer to the metal oxide surface. In 2, the photoexcited electron must travel through the intervening phenyl group to reach the surface, resulting in slower electron injection. A similar trend in electron injection lifetimes was observed for increasing surface linker lengths in porphyrins.³³ Measurements were also taken at 40 mW power to ensure against photodegradation of the samples (Figure S11-S14 and Table S2). Due to the lower signal in the measurements taken at 40 mW, the fit parameters have a large variance, but these measurements exhibit a similar trend in electron injection lifetimes.

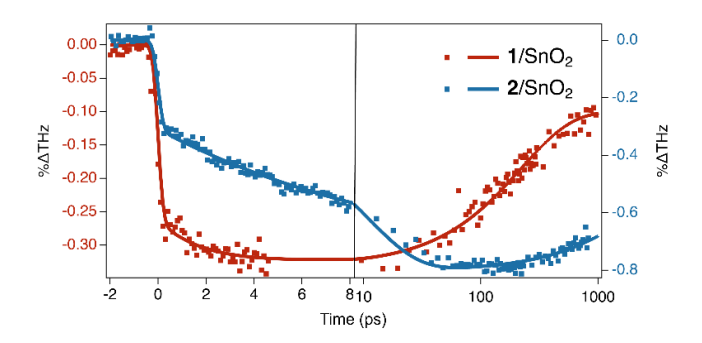


Figure 3. Representative OPTP data of 1/SnO₂ (plotted on the left-axis scale) and 2/SnO₂ (plotted on the right-axis scale). Terahertz data are plotted as square markers, whereas fitted models are plotted as solid lines. Samples shown were measured at a power of 100 mW.

Table 2. Fit parameters for OPTP traces photoexcited with 100 mW 400 nm excitation pulse using Equation 1 (see Experimental Methods).^a

	t_i (ps)	β	$< t_i > b$ (ps)	t_r (ps)
1/SnO ₂	3.855	0.8711	4.304	288.6
	(1.797, 5.912)	(0.7877, 0.9545)	(1.835, 6.774)	(355.4, 221.7)
2 /SnO ₂	9.155	0.9749	9.251	1509
	(7.539, 10.770)	(0.9829, 0.9668)	(7.652, 10.850)	(1000, 2018)

^aThe average values are reported and the fit values of the individual traces are in parentheses. ^bThe average electron injection lifetimes were obtained using Equation 2 (see Experimental Methods).

Smaller values of β were found for 1/SnO₂, which indicate a less uniform electron injection process that may be related to heterogeneity of binding modes. The variance in recombination/trapping lifetimes (t_r) was too large to draw definite conclusions, especially at low power, although samples of 2/SnO₂ generally had slower charge trapping or recombination. Better accuracy on the recombination could be achieved by extending the measurement time, which was not possible on the spectrometer used for these studies. Differences in amplitudes from the fits were not interpreted due to the contribution of direct excitation within the SnO₂ that was not modeled.

Direct band-gap excitation in bare SnO₂ is instrument-response limited (Figure S15), supporting the conclusion that the observed electron injection on a longer timescale in the OPTP

traces of dye-sensitized SnO₂ occurred from photosensitizer LUMO into the SnO₂ conduction band. Overall, the OPTP data show that 1 is at least, if not more, effective than 2 for application in photoanodes in combination with large band-gap semiconductors, due to its quicker electron injection. The fast electron injection of 1 could also prevent electron recombination within the dye.

Electron injection from the dyes into SnO₂ was also monitored using transient absorption (TA) spectroscopy. In the THz measurements, the electron injection into the bulk semiconductor is observed; while with the same wavelength excitation, a clear photoexcitation and subsequent oxidation of 1 and 2 is seen in the TA measurement (Figure S16). A bleach of the characteristic ground state features at 514 nm and 548 nm, respectively, arise within ~5 ps upon photoexcitation of 1 and 2. Electron injection lifetimes could not be extracted from the TA time traces due to multiple excitation, oxidation, and recombination processes. However, oxidized species lifetimes on the order of 1-5 ns are in broad agreement with charge recombination dynamics measured by OPTP. There is also an observable feature at lower energies which grows in (Figure S16) and can be attributed to the oxidized species, as seen in the spectroelectrochemistry experiments (Figure S2). The results from these spectroscopic methods confirm that 1 is a competent dye and anchoring group for DSPECs.

Quantum Chemistry Calculations

Due to the THz instrument response limitations on sensitized TiO₂, the preferred semiconductor substrate for DSPECs, an *in-silico* approach was applied to investigate the electron injection pathways between dye and TiO₂ semiconductor. The photoinduced interfacial electron transfer (IET) can be tracked in real time with a hybrid quantum classical approach that combines GFN-xTB based nuclear dynamics with quantum dynamics simulations of the electronic

relaxation. Figure 4a shows the electron population transferring from 1 to the TiO₂ surface revealing one of the paths for photoinduced electron transfer.

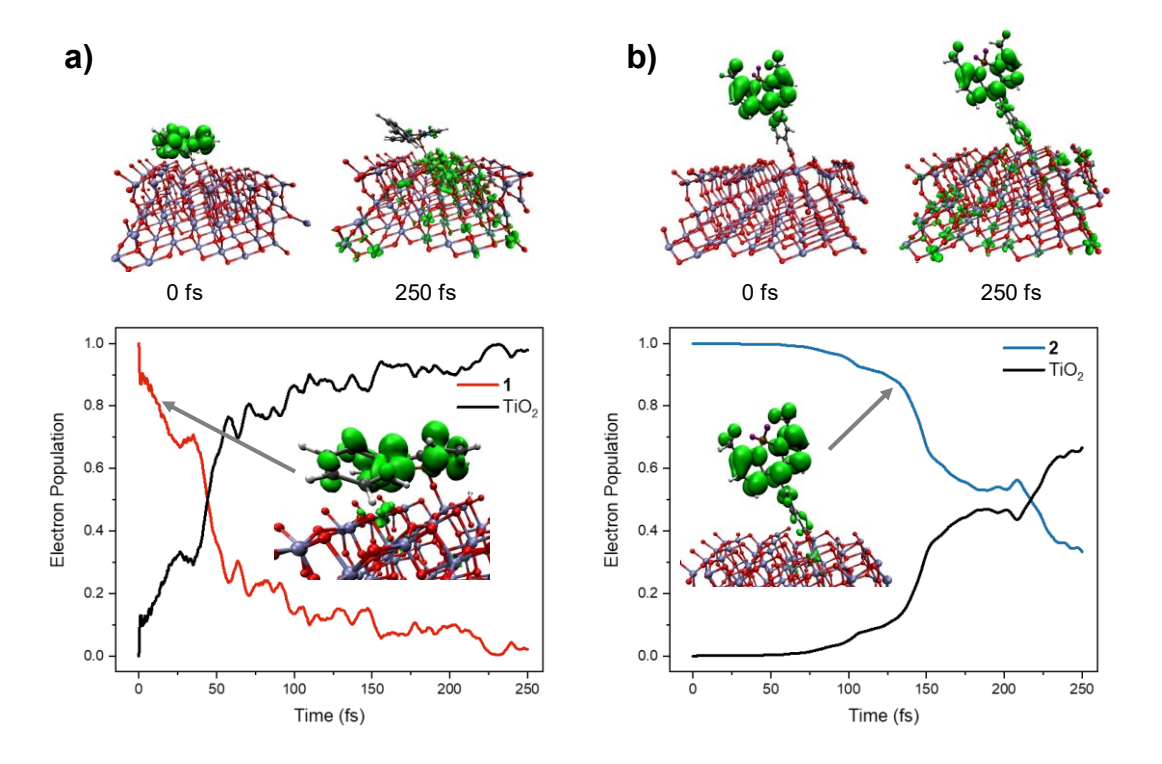


Figure 4. a) Electron injection over time for one example trajectory in the $1/\text{TiO}_2$ system; the electron population on 1 (red), decreases while the population on TiO_2 (black) increases. On top, the electron density is shown in green at initial time (0 fs) and the final step in the simulation (250 fs) with the electron fully injected into TiO_2 . The inset shows the electron density at the initial electron injection time point, with direct electron injection from the π -system into a Ti d-orbital. b) Electron injection over time for one example trajectory in the $2/\text{TiO}_2$ system; the electron population on 2 (blue) decreases while the population on TiO_2 (black) increases. On top, the electron density is shown in green at initial time (0 fs) and the final step in the simulation (250 fs) with the electron fully injected into TiO_2 . The inset shows the onset of electron injection, where the electron density has to migrate through the phenyl group of 2 before being injected into the electrode.

Initially, the electron is fully localized on 1, specifically in its LUMO, as also shown in the inset. Upon time propagation, the electron is readily transferred from 1 into the TiO₂ electrode, with full electron injection within the first 175 fs, where it remains as also evident from the electron distribution after 250 fs. In Figure 4b, the same is given for 2, where electron injection is also observed, but with a significant delay.

These results already show that 1 might outperform 2 in terms of the IET dynamics and are consistent with the analysis of IET from 1 and 2 over time, averaged over multiple trajectories. Averaging over ten trajectories give the mean electron population dynamics on 1 and 2 over time (Figure 5a). The corresponding mean electron populations on all fragments and the resulting standard deviations are provided in the SI (Figures S17a-S18a and S17b-S18b).

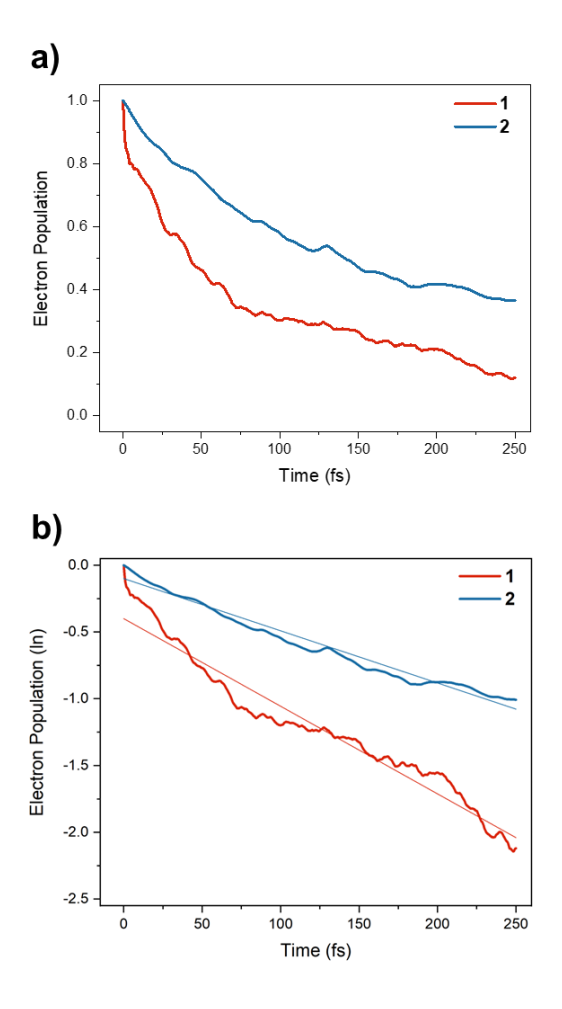


Figure 5. a) Mean Electron population on 1 (red) and 2 (blue) over time, averaged over all ten trajectories. b) Mean Electron population on 1 (red) and 2 (blue) averaged over ten trajectories each as a semi-logarithmic plot. The thin lines represent a linear fit which for 1 is y = -0.00656x - 0.4 and for 2 is y = -0.00391x - 0.1.

In agreement with experiment where the electron injection into TiO₂ is faster than the instrument response time of 400 fs, both compounds display ultrafast electron injection of the photoexcited electron into the TiO₂ electrode. While 1 injects within approximately 250 fs, 2

injects about 60% of the electron within the first 250 fs. When plotting the mean population on the dye fragment over time on a semi-logarithmic scale, a linear fit can be used to estimate the electron injection rate (Figure 5b, Table S3). In agreement with the THz results of both compounds on SnO₂, **1** injects more than 50% faster than **2**.

These results are surprising since the excited state energies of the two compounds are quite similar, with 2 displaying a slightly higher LUMO energy. Therefore, we have investigated the individual quantum dynamics trajectories. We find that electron injection from 2 is more sensitive to the different conditions giving rise to the trajectories, such as the specific molecular conformations, as can also be seen when comparing the traces of all trajectories (Figure S17-18). There are several cases where almost no electron injection is observed, until a sudden decrease in electron population occurs. This suggests that particular conformations are needed for 2 to inject. To investigate this further, a closer look at the trajectories for 1 and 2, shown in Figure 4, is necessary. The insets of Figure 4 show the electron distribution at the onset of the electron injection process. Compound 1 readily injects, with the initial transfer of electron density from the BODIPY backbone that is closely coupled to the surface, into a d orbital of a surface Ti. In contrast, no electron injection from 2 is observed until around 100 fs after which the electron injection proceeds very quickly.

The electron density of the LUMO of 2, which is also in the BODIPY backbone, migrates through the π -system of the phenyl ring and the carboxylate before reaching the TiO₂, making the electron injection very dependent on the conjugation and the dihedral angles of the system. Full movies of the electron injection of the two example trajectories are provided in the SI. The different behavior is determined by the binding mode of 1, where direct attachment through boron atoms leads to a closely coupled dye-electrode complex. In comparison, 2 requires a specific range of

conformations to inject, as revealed from the different electron injection pathways and the larger distribution of trajectories (i.e., larger standard deviation). Even though both processes are ultrafast, a distinct difference in the electron injection behavior is noticeable. It is remarkable that the attachment via boron is on the same order of magnitude and even surpassing the electron injection rates mediated by the carboxylate, known to be an anchor that allows for ultrafast IET. *Stability in Acidic and Basic Environments*

Water oxidation catalysts require various specific conditions for optimal activity, with some such as copper based catalysts performing best in basic conditions, ⁴² while others, such as iridium catalysts are optimal in acidic conditions. ⁴³ It is important for the anchoring group to be stable in aqueous conditions that match the pH being used. To determine the range of stability for 1/TiO₂, the film was submerged in 0.1 M solutions of KCl which were adjusted to pH 2, 7, and 10. As seen in Figure 6, over 24 hours there is significantly improved stability for 1/TiO₂ compared with 2/TiO₂ across all pH conditions. The difference is more dramatic at pH 7 and 10 where carboxylic acids are known to not be stable, but even in acidic conditions 1 suffers only 30% loss over 24 hours compared with 2 at 80% loss.

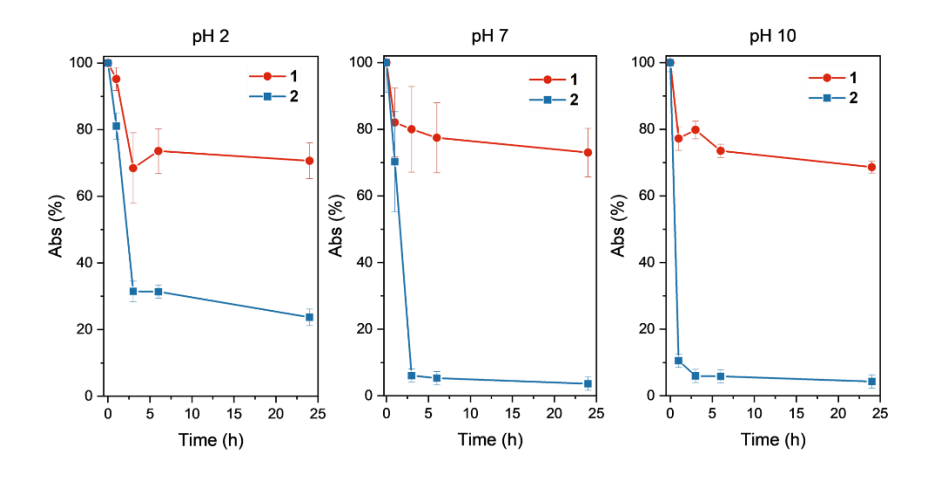


Figure 6. Stability of 1/TiO₂ and 2/TiO₂ at different pH conditions.

Interestingly, the loss is not linear with time for either dye. This suggests that there are two or more different modes of attachment, potentially an amount is physisorbed and weakly attached which comes off quickly in the first few hours, leaving the more robust covalently bound species which remains stable for longer. This is further supported by a difference in stability that was found based on how heavily loaded the samples were. The standard absorption of 1 on a 4-µm thick film is ~0.4 arbitrary units; however, some films exhibited higher absorptions of ~1.0 arbitrary units. These films present higher instability which results in the loss of more than 60% of the absorbed dye after one hour at pH 2. This leads to the same amount of dye remaining on the surface as the standard absorption film after the same amount of time (Figure S19). This behavior may be associated with different non-covalent interactions such as physisorption, stacking due to the highly aromatic molecular structure of the dye, or alternate covalent binding modes. Unfortunately, due to the weak attachment of metal oxides onto the quartz substrates used in the THz experiments we were not able to directly probe if there are differences in the injection of these weaker and stronger binding modes.

Photoelectrochemistry

The ability and the performance of the dye-sensitized photoanodes in converting photons into electrons is measured with photoelectrochemical studies in the dark versus under illumination in the presence of a SED.⁸ In our case, the photoelectrochemical measurements were performed using a three-electrode electrochemical cell in a phosphate buffer solution at pH 7 using Na₂SO₃ as the SED. The response of each photosystem in the linear sweep voltammetry (LSV) under chopped illumination confirmed the photoactive behaviors (Figure S20). Due to the high difference in the generated photocurrent at 0 V vs Ag/AgCl with respect to the dark current, this bias was in the following electrolysis. At the pH 7 conditions we are using, this is a bias of about 600 mV vs

reversible hydrogen electrode (RHE). The dye-sensitized photoanodes were measured for five minutes both in the presence and absence of the SED under chopped illumination. To maintain the correct buffer strength in the control experiments, the concentration of the phosphate buffer was increased from 0.075 M to 0.1 M.

As shown in Figure 7, both films generated a remarkably higher photocurrent in the presence of the SED. 1/TiO₂ presented a photocurrent of 5.32 μA cm⁻² at the beginning of the measurement which decreased by 40% over five minutes. On the other hand, 2/TiO₂ produced a higher photocurrent in the first few minutes, but its low stability in neutral pH caused a drop in the photocurrent of about 90% after five minutes. At this timepoint, the current for 2/TiO₂ with and without SED present are the same, suggesting that this current is due to the oxidation of 2 itself. Interestingly, 2/TiO₂ without SED also shows a relatively high current density (~ 15 μA cm⁻²) in the first minute which suggests that the photoexcited dye is self-oxidizing. In the case of 1/TiO₂, when there is no SED present, the current is comparable with the bare TiO₂ (Figure S21) suggesting this is an oxidation resistant anchoring mode.

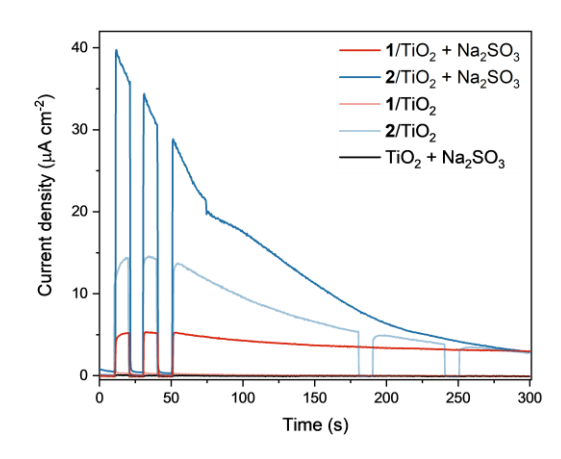


Figure 7. CA of the dye-sensitized TiO₂ films in a 0.1 M phosphate buffer solution at pH 7 in the presence of Na₂SO₃ as an irreversible SED under irradiation (100 mW cm⁻² filtered with $\lambda > 420$ nm) with an external bias of 0 V vs Ag/AgCl (KCl sat.).

The difference in initial photocurrent between 1/TiO₂ and 2/TiO₂ in the case of the Na₂SO₃ oxidation can be in large part attributed to the difference in absorbance of the different electrodes (Figure S22). 2 loads onto TiO₂ about three times as many molecules on a given area as 1, and the molar extinction coefficient of 2 is also twice that of 1. This leads to about six times more photons being absorbed in the case of 2/TiO₂. The remaining difference could be explained by the presence of more back electron transfer reactions from the semiconductor due to the presumed parallel orientation of 1 on the surface. In the case of both 1 and 2, the HOMO and LUMO are placed on the dipyrrin scaffold and overlap, promoting recombination reactions that compete with the electron injection.³⁴ The faster recombination and back electron transfer from the TiO₂ results in less oxidized dye being available for substrate oxidation.

The stability of the photoanodes have also been evaluated during a two-hour CA (Figures S23-24). After only 550 s, the photocurrent of 2/TiO₂ dropped below the current density of 1/TiO₂. At the end of the measurement, 1/TiO₂ still produced a distinct photocurrent while the 2/TiO₂ sample has become comparable to a blank slide.

Effects of Additives on BODIPY Loading

To improve the loading of 1 onto metal oxide surfaces for further applications it is useful to understand what factors can influence the loading. We previously reported that using dry glassware and solvents is important for high loading.¹⁶ Here we investigate other additives and their effect on the binding of 1/TiO₂ when all other conditions are kept constant.

The addition of acid to the sensitizing solution decreased the loading of 1 both in the case when acetic acid (AcOH) a protic, non-aromatic acid was used, and when 3,5-bis(trifluoromethyl)phenol (PhenolCF₃) a protic, aromatic acid was used. When bases were added, there was modest improvement in loading in some cases, but not beyond the sample error (Figure

S25). The bases used included pyridine, *N*,*N*-diisopropylethylamine (DIPEA), and 1,4-diazabicyclo[2.2.2]octane (DABCO) chosen to cover a range of aromaticity and nucleophilicity.

In the case of 1/TiO₂, adding a fluoride source in the form of tetrabutylammonium fluoride (TBAF) to the sensitizing solution entirely shut off loading (Figure 8). This same effect was not seen when the TiO₂ films were pre-sensitized with fluoride either in the form of TBAF in acetonitrile or potassium fluoride in water (Figure S26). Additionally, this change in loading was not seen in the case of 2/TiO₂ with TBAF (Figure S26). In this instance, an increase in loading was observed, though this could be due to error in measurement since the absorbance is significantly close to the detection limit of the spectrophotometer. These observations could suggest that the rate limiting step for the mechanism of 1 loading onto TiO₂ includes the loss of a fluoride ligand from BODIPY prior to binding to a surface oxygen species. The presence of excess fluoride in solution disfavors this ligand loss and thus prevents binding to the surface. Boron is known to have the ability to form hypervalent species, ⁴⁴ so it is still possible for this surface attachment to proceed via either a S_N1 or S_N2 mechanism, and further computational and experimental evidence would be necessary to determine the exact mechanism.

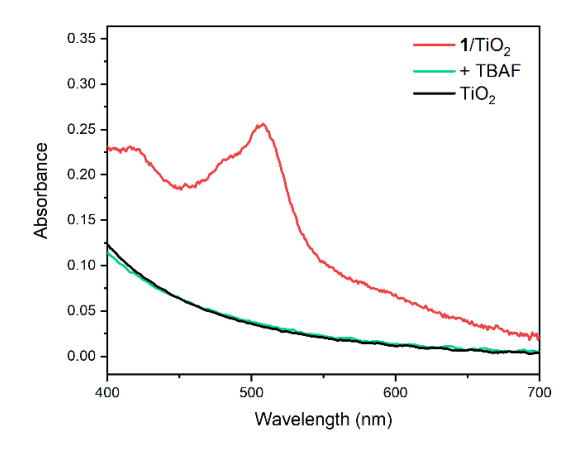


Figure 8. UV-visible spectra of 1/TiO₂ obtained from a sensitization solution containing 1 mM TBAF. A bare TiO₂ film and 1/TiO₂ sensitized under typical conditions are included for reference.

Conclusions

A durable dye-sensitized photoanode requires ultrafast electron injection, stability in aqueous environments, and resistance to oxidation. Both 1 and 2 have appropriate energy levels for electron injection into metal oxide semiconductors such as TiO₂ and SnO₂ as well as suitable oxidation potentials to drive water oxidation. Electron injection dynamics were investigated through THz and TA spectroscopy. Notably, 1 injects electrons into the conduction band of SnO₂ roughly twice as fast as 2 and this finding was also corroborated by computation studies which demonstrate that this difference holds true for these dyes on TiO₂.

The facile electron injection and wide use of carboxylic acid anchoring groups are well-known in the literature of DSPECs. The fact that this new anchoring group at least matches the capability of the carboxylic acid in electron injection suggests promising future applications. In addition, 1 greatly surpasses 2 in terms of stability in aqueous environments. 1/TiO₂ is more stable than 2/TiO₂ in all the different pHs tested (2, 7, and 10). This range of pH values is important because it allows for flexibility in the choice of the water oxidation catalysts and reactions that the photoanode is used for. Although the surface coverage of 1 is lower than 2, at long times it exhibits a greater photocurrent for oxidation when using a SED due in large part to the improved stability towards oxidation and in aqueous environments.

Future works on increasing the surface coverage with 1 is necessary to improve the performance of any devices. Unlike other anchoring groups,⁴⁵ the addition of acids or bases did not so far significantly increase the loading on TiO₂. In the case that additives are successful in increasing loading it will be necessary to control for any other changes the additives may have such as shifting the conduction band of the metal oxide. Further efforts are now being spent in changing the dye structure to improve the HOMO-LUMO separation of the dye and introduce

conformational effects to prevent the rapid charge recombination, identified in both the spectroscopy experiments and the computations.⁴⁶

Supporting Information

Details on spectroscopic methods; spectroelectrochemistry results; NMR spectra; additional THz and TA spectra and fits; quantum chemistry electron injection trajectories and methods; photoelectrochemistry voltammograms; and additional UV-vis spectra (PDF). Interfacial Electron Transfer Movies for Compounds 1 and 2 (.avi). The Supporting Information is available free of charge at https://pubs.acs.org/doi/XXX.

Author Contributions

The manuscript was written through contributions of all authors. All authors have given approval to the final version of the manuscript. ‡These authors contributed equally.

Funding Sources

This work was supported by the U.S. Department of Energy, Chemical Sciences, Geosciences, and Biosciences Division, Office of Basic Energy Sciences, Office of Science (Grant DE-FG02-07ER15909). P.G. acknowledges the support by the National Science Foundation under Grant CHE-2305138. V.B. and J.P.M used resources of the National Energy Research Scientific Computing Center (NERSC), a U.S. Department of Energy Office of Science User Facility located at Lawrence Berkeley National Laboratory, operated under Contract No. DE-AC02-05CH11231 using NERSC award BES-ERCAP0024594. Additional support was provided by a generous donation from the TomKat Charitable Trust.

References

- Barber, J. and Tran, P. D. From Natural to Artificial Photosynthesis. *J. R. Soc. Interface* **10**, 20120984 (2013). https://doi.org/doi:10.1098/rsif.2012.0984
- Wang, Z., Hu, Y., Zhang, S., and Sun, Y. Artificial Photosynthesis Systems for Solar Energy Conversion and Storage: Platforms and Their Realities. *Chem. Soc. Rev.* **51**, 6704-6737 (2022). https://doi.org/10.1039/D1CS01008E
- Vlachopoulos, N. and Hagfeldt, A. Photoelectrochemical Cells Based on Dye Sensitization for Electricity and Fuel Production. *CHIMIA* 73, 894-905 (2019). https://doi.org/10.2533/chimia.2019.894
- Zhang, S., Ye, H., Hua, J., and Tian, H. Recent Advances in Dye-Sensitized Photoelectrochemical Cells for Water Splitting. *EnergyChem* 1, 100015 (2019). https://doi.org/https://doi.org/10.1016/j.enchem.2019.100015
- Swierk, J. R. and Mallouk, T. E. Design and Development of Photoanodes for Water-Splitting Dye-Sensitized Photoelectrochemical Cells. *Chem. Soc. Rev.* **42**, 2357-2387 (2013). https://doi.org/10.1039/C2CS35246J
- Zhang, B. and Sun, L. Artificial Photosynthesis: Opportunities and Challenges of Molecular Catalysts. *Chem. Soc. Rev.* **48**, 2216-2264 (2019). https://doi.org/10.1039/C8CS00897C
- Collomb, M.-N., Morales, D. V., Astudillo, C. N., Dautreppe, B., and Fortage, J. Hybrid Photoanodes for Water Oxidation Combining a Molecular Photosensitizer with a Metal Oxide Oxygen-Evolving Catalyst. *Sustain. Energy Fuels* **4**, 31-49 (2020). https://doi.org/10.1039/C9SE00597H
- Decavoli, C., Boldrini, C. L., Manfredi, N., and Abbotto, A. Molecular Organic Sensitizers for Photoelectrochemical Water Splitting. *Eur. J. Inorg. Chem.*, 978-999 (2020). https://doi.org/10.1002/ejic.202000026
- Warnan, J. and Reisner, E. Synthetic Organic Design for Solar Fuel Systems. *Angew. Chem. Int. Ed.* **59**, 17344-17354 (2020). https://doi.org/https://doi.org/10.1002/anie.202006013
- Materna, K. L., Crabtree, R. H., and Brudvig, G. W. Anchoring Groups for Photocatalytic Water Oxidation on Metal Oxide Surfaces. *Chem. Soc. Rev.* **46**, 6099-6110 (2017). https://doi.org/10.1039/C7CS00314E
- Ding, X.; Zhang, L.; Wang, Y.; Liu, A.; Gao, Y., Design of Photoanode-Based Dye-Sensitized Photoelectrochemical Cells Assembling with Transition Metal Complexes for Visible Light-Induced Water Splitting. *Coord. Chem. Rev.* **357**, 130-143 (2018). https://doi.org/10.1016/j.ccr.2017.10.020
- Liu, H.-Y., Cody, C. C., Jayworth, J. A., Crabtree, R. H., and Brudvig, G. W. Surface-Attached Molecular Catalysts on Visible-Light-Absorbing Semiconductors: Opportunities and Challenges for a Stable Hybrid Water-Splitting Photoanode. *ACS Energy Lett.* **5**, 3195-3202 (2020). https://doi.org/10.1021/acsenergylett.0c01719

- Zhang, L. and Cole, J. M. Anchoring Groups for Dye-Sensitized Solar Cells. *ACS Appl. Mater. Interfaces* 7, 3427-3455 (2015). https://doi.org/10.1021/am507334m
- Badgurjar, D., Shan, B., Nayak, A., Wu, L., Chitta, R., and Meyer, T. J. Electron-Withdrawing Boron Dipyrromethene Dyes As Visible Light Absorber/Sensitizers on Semiconductor Oxide Surfaces. *ACS Appl. Mater. Interfaces* **12**, 7768-7776 (2020). https://doi.org/10.1021/acsami.9b20167
- Higashino, T., Kurumisawa, Y., Cai, N., Fujimori, Y., Tsuji, Y., Nimura, S., Packwood, D. M., Park, J., and Imahori, H. A Hydroxamic Acid Anchoring Group for Durable Dye-Sensitized Solar Cells Incorporating a Cobalt Redox Shuttle. *ChemSusChem* **10**, 3347-3351 (2017). https://doi.org/10.1002/cssc.201701157
- Jayworth, J. A., Capobianco, M. D., Liu, H.-Y., Decavoli, C., Crabtree, R. H., and Brudvig, G. W. BODIPY and Dipyrrin as Unexpected Robust Anchoring Groups on TiO₂ Nanoparticles. *Dalton Trans.* **51**, 14260-14266 (2022). https://doi.org/10.1039/D2DT02116A
- Suryani, O., Higashino, Y., Mulyana, J. Y., Kaneko, M., Hoshi, T., Shigaki, K., and Kubo, Y. A Near-Infrared Organic Photosensitizer for Use in Dye-Sensitized Photoelectrochemical Water Splitting. *Chem. Commun.* **53**, 6784-6787 (2017). https://doi.org/10.1039/C7CC02730C
- Suryani, O., Higashino, Y., Sato, H., and Kubo, Y. Visible-to-Near-Infrared Light-Driven Photocatalytic Hydrogen Production Using Dibenzo-BODIPY and Phenothiazine Conjugate as Organic Photosensitizer. *ACS Appl. Energy Mater.* **2**, 448-458 (2019). https://doi.org/10.1021/acsaem.8b01474
- Nikolaou, V., Charalambidis, G., Landrou, G., Nikoloudakis, E., Planchat, A., Tsalameni, R., Junghans, K., Kahnt, A., Odobel, F., and Coutsolelos, A. G. Antenna Effect in BODIPY-(Zn)Porphyrin Entities Promotes H₂ Evolution in Dye-Sensitized Photocatalytic Systems. *ACS Appl. Energy Mater.* **4**, 10042-10049 (2021). https://doi.org/10.1021/acsaem.1c01975
- Syrek, K., Czopor, J., Topa-Skwarczyńska, M., Pilch, M., Kamiński, K., Ortyl, J., and Sulka, G. D. Photoelectrochemical Properties of BODIPY-Sensitized Anodic TiO₂ Layers Decorated with AuNPs for Enhanced Solar Performance. *J. Phys. Chem. C* **127**, 9471-9480 (2023). https://doi.org/10.1021/acs.jpcc.3c00931
- Jiang, J., Swierk, J. R., Materna, K. L., Hedström, S., Lee, S. H., Crabtree, R. H., Schmuttenmaer, C. A., Batista, V. S., and Brudvig, G. W. High-Potential Porphyrins Supported on SnO₂ and TiO₂ Surfaces for Photoelectrochemical Applications. *J. Phys. Chem. C* **120**, 28971-28982 (2016). https://doi.org/10.1021/acs.jpcc.6b10350
- Kolemen, S., Bozdemir, O. A., Cakmak, Y., Barin, G., Erten-Ela, S., Marszalek, M., Yum, J.-H., Zakeeruddin, S. M., Nazeeruddin, M. K., Grätzel, M., and Akkaya, E. U. Optimization of Distyryl-Bodipy Chromophores for Efficient Panchromatic Sensitization in Dye Sensitized Solar Cells. *Chem. Sci.* **2**, 949-954 (2011). https://doi.org/10.1039/C0SC00649A
- Smith, C. D. and Thompson, A. Facile Deprotection of F-BODIPYs Using Methylboronic Acid. *RSC Adv.* **10**, 24273-24279 (2020). https://doi.org/10.1039/D0RA05151A

- Ito, S., Chen, P., Comte, P., Nazeeruddin, M. K., Liska, P., Péchy, P., and Grätzel, M. Fabrication of Screen-Printing Pastes from TiO₂ Powders for Dye-Sensitised Solar Cells. *Prog. Phot. Res. Appl.* **15**, 603-612 (2007). https://doi.org/10.1002/pip.768
- Monti, A., Negre, C. F. A., Batista, V. S., Rego, L. G. C., de Groot, H. J. M., and Buda, F. Crucial Role of Nuclear Dynamics for Electron Injection in a Dye–Semiconductor Complex. *J. Phys. Chem. Lett.* **6**, 2393-2398 (2015). https://doi.org/10.1021/acs.jpclett.5b00876
- da Silva, R., Hoff, D. A., and Rego, L. G. C. Coupled Quantum-Classical Method for Long Range Charge Transfer: Relevance of the Nuclear Motion to the Quantum Electron Dynamics. *J. Phys. Condens. Matter* **27**, 134206 (2015). https://doi.org/10.1088/0953-8984/27/13/134206
- 27 Rego, L. G. C. and Batista, V. S. Quantum Dynamics Simulations of Interfacial Electron Transfer in Sensitized TiO₂ Semiconductors. *J. Am. Chem. Soc.* **125**, 7989-7997 (2003). https://doi.org/10.1021/ja0346330
- Menzel, J. P., Boeije, Y., Bakker, T. M. A., Belić, J., Reek, J. N. H., de Groot, H. J. M., Visscher, L., and Buda, F. In Silico Optimization of Charge Separating Dyes for Solar Energy Conversion. *ChemSusChem* **15**, e202200594 (2022). https://doi.org/https://doi.org/10.1002/cssc.202200594
- Menzel, J. P., Papadopoulos, A., Belić, J., de Groot, H. J. M., Visscher, L., and Buda, F. Photoinduced Electron Injection in a Fully Solvated Dye-Sensitized Photoanode: A Dynamical Semiempirical Study. *J. Phys. Chem. C* **124**, 27965-27976 (2020). https://doi.org/10.1021/acs.jpcc.0c09551
- Hourahine, B., Aradi, B., Blum, V., Bonafé, F., Buccheri, A., Camacho, C., Cevallos, C., Deshaye, M. Y., Dumitrică, T., Dominguez, A., Ehlert, S., Elstner, M., van der Heide, T., Hermann, J., Irle, S., Kranz, J. J., Köhler, C., Kowalczyk, T., Kubař, T., Lee, I. S., Lutsker, V., Maurer, R. J., Min, S. K., Mitchell, I., Negre, C., Niehaus, T. A., Niklasson, A. M. N., Page, A. J., Pecchia, A., Penazzi, G., Persson, M. P., Řezáč, J., Sánchez, C. G., Sternberg, M., Stöhr, M., Stuckenberg, F., Tkatchenko, A., Yu, V. W.-z., and Frauenheim, T. DFTB+, a Software Package for Efficient Approximate Density Functional Theory Based Atomistic Simulations. *J. Chem. Phys.* 152 (2020). https://doi.org/10.1063/1.5143190
- Grimme, S., Bannwarth, C., and Shushkov, P. A Robust and Accurate Tight-Binding Quantum Chemical Method for Structures, Vibrational Frequencies, and Noncovalent Interactions of Large Molecular Systems Parametrized for All spd-Block Elements (*Z* = 1–86). *J. Chem. Theory Comput.* **13**, 1989-2009 (2017). https://doi.org/10.1021/acs.jctc.7b00118
- Martyna, G. J., Tuckerman, M. E., Tobias, D. J., and Klein, M. L. Explicit Reversible Integrators for Extended Systems Dynamics. *Mol. Phys.* **87**, 1117-1157 (1996). https://doi.org/10.1080/00268979600100761
- Lee, S. H., Regan, K. P., Hedström, S., Matula, A. J., Chaudhuri, S., Crabtree, R. H., Batista, V. S., Schmuttenmaer, C. A., and Brudvig, G. W. Linker Length-Dependent Electron-Injection Dynamics of Trimesitylporphyrins on SnO₂ Films. *J. Phys. Chem. C* **121**, 22690-22699 (2017). https://doi.org/10.1021/acs.jpcc.7b07855
- Jiang, J., Spies, J. A., Swierk, J. R., Matula, A. J., Regan, K. P., Romano, N., Brennan, B. J., Crabtree, R. H., Batista, V. S., Schmuttenmaer, C. A., and Brudvig, G. W. Direct Interfacial Electron Transfer from High-Potential Porphyrins into Semiconductor Surfaces: A Comparison of

- Linkers and Anchoring Groups. *J. Phys. Chem. C* **122**, 13529-13539 (2018). https://doi.org/10.1021/acs.jpcc.7b12405
- Wu, Q. and Zhang, X. C. Free-Space Electro-Optic Sampling of Terahertz Beams. *Appl. Phys. Lett.* **67**, 3523-3525 (1995). https://doi.org/10.1063/1.114909
- Capobianco, M. D., Pattengale, B., Neu, J., and Schmuttenmaer, C. A. Single Copper Atoms Enhance Photoconductivity in *g*-C₃N₄. *J. Phys. Chem. Lett.* **11**, 8873-8879 (2020). https://doi.org/10.1021/acs.jpclett.0c02756
- Pavlishchuk, V. V. and Addison, A. W. Conversion Constants for Redox Potentials Measured versus Different Reference Electrodes in Acetonitrile Solutions at 25 °C. *Inorg. Chim. Acta* **298**, 97-102 (2000). https://doi.org/https://doi.org/10.1016/S0020-1693(99)00407-7
- Loudet, A. and Burgess, K. BODIPY Dyes and Their Derivatives: Syntheses and Spectroscopic Properties. *Chem. Rev.* **107**, 4891-4932 (2007). https://doi.org/10.1021/cr078381n
- Lovell, T. C.; Branchaud, B. P.; Jasti, R., An Organic Chemist's Guide to Fluorophores Understanding Common and Newer Non-Planar Fluorescent Molecules for Biological Applications. Eur J Org Chem (2024). https://doi.org/10.1002/ejoc.202301196
- Mukherjee, S.; Thilagar, P., Effect of Alkyl Substituents in BODIPYs: A Comparative DFT Computational Investigation. RSC Adv., **5**, 2706-2714 (2015). https://doi.org/10.1039/C4RA12071J
- Tiwana, P., Docampo, P., Johnston, M. B., Snaith, H. J., and Herz, L. M. Electron Mobility and Injection Dynamics in Mesoporous ZnO, SnO₂, and TiO₂ Films Used in Dye-Sensitized Solar Cells. *ACS Nano* 5, 5158-5166 (2011). https://doi.org/10.1021/nn201243y
- Fisher, K. J., Materna, K. L., Mercado, B. Q., Crabtree, R. H., and Brudvig, G. W. Electrocatalytic Water Oxidation by a Copper(II) Complex of an Oxidation-Resistant Ligand. *ACS Catal.* 7, 3384-3387 (2017). https://doi.org/10.1021/acscatal.7b00494
- Thomsen, J. M., Huang, D. L., Crabtree, R. H., and Brudvig, G. W. Iridium-based Complexes for Water Oxidation. *Dalton Trans.* 44, 12452-12472 (2015). https://doi.org/10.1039/C5DT00863H
- Hirano, Y., Kojima, S., and Yamamoto, Y. A Hypervalent Pentacoordinate Boron Compound with an N–B–N Three-Center Four-Electron Bond. *J. Org. Chem.* **76**, 2123-2131 (2011). https://doi.org/10.1021/jo1024656
- Troiano, J. L., Crabtree, R. H., and Brudvig, G. W. Optimization of Surface Loading of the Silatrane Anchoring Group on TiO₂. *ACS Appl. Mater. Interfaces* **14**, 6582-6589 (2022). https://doi.org/10.1021/acsami.1c20678
- Spettel, K. E.; Damrauer, N. H., Exploiting Conformational Dynamics of Structurally Tuned Aryl-Substituted Terpyridyl Ruthenium(II) Complexes to Inhibit Charge Recombination in Dye-Sensitized Solar Cells. *J. Phys. Chem. C*, **20**, 10815-10829 (2016). https://doi.org/10.1021/acs.jpcc.6b03302

For Table of Contents Only

